

Chapter 1

Theory

In this chapter we review and develop the theory required to model signal transmission from cosmic source to data product. The first half of this chapter is a broad section centred around radio interferometric concepts while the second half is focused specifically on describing several key signal corruptions.

1.1 Radio Interferometry

This section is structured as follows: first radio interferometry is introduced using the Radio Interferometric Measurement Equation (RIME) formalism, which serves as a guiding framework for the construction of the MEQSILOUETTE simulator; following on, we review the technique of self-calibration which is important as it's effects are strongly linked with the signal corruptions, particularly those associated with the troposphere; we then discuss typical mm-VLBI data products and the consequences of breaking the static source assumption.

1.1.1 Measurement Equation

The RIME provides the notation and formalism to model the signal transmission path as a sequence of linear operations. Specifically, it takes into account polarisation, correlation and the correct time-ordering of signal transmission path in an intuitive and efficient way. This calculus will also enable a more informative phrasing of the relation between calibration and signal corruptions.

Here we offer a short derivation and explanation of the RIME following

?]. Consider a quasi-monochromatic complex valued electric field vector \mathbf{E} , which can be decomposed into an arbitrary two dimensional orthogonal basis in the plane perpendicular to the direction of propagation,

$$\mathbf{E} = \begin{pmatrix} E_a \\ E_b \end{pmatrix}.$$

where this choice represents the basis in which the polarisation is measured. All linear transformations of the above electric field can be written by a multiplication with a 2 x 2 complex valued matrix, termed a *Jones* matrix ,

$$\mathbf{E}' = \mathbf{J}\mathbf{E}. \quad (1.1)$$

For example the conversion of the electric field to a voltage \mathbf{v} at an antenna can be specified by such a transformation i.e. $\mathbf{v} \equiv \mathbf{E}'$ under multiplication with the appropriate \mathbf{J} . Multiple effects then can be represented by multiplication of various Jones matrices, forming a Jones chain,

$$\mathbf{E}' = \mathbf{J}_n \dots \mathbf{J}_1 \mathbf{E}. \quad (1.2)$$

The order of the Jones matrices should obey the casual order of the signal transmission path. However the rules of commutivity of matrices allows us some flexibility. Matrices which are scalar commute with everything, while diagonal matrices commute with each other as do matrices which effect a rotation of \mathbf{E} . This allows the Jones chain to be re-ordered into more convenient formulations as required. In other words, the signal path can be parameterised in different ways. For example during calibration, one could construct a *phenomenological* Jones matrix which represents the combined action of several *physical* commuting processes/matrices. The advantage would be that only the cumulative effect is considered, which keeps the number of parameters to solve for to a minimum. This would be useful when the individual effects cannot be distinguished anyway. On the other hand, for realistic data simulation, we prefer to model the signal transmission path by formulating a Jones matrix based on physics.

An interferometer measures the correlation of the voltages from an antenna pair or *baseline*. The correlator output is termed the *visibility*,

$$V_{pq} = \langle \mathbf{v}_p \mathbf{v}_q^H \rangle, \quad (1.3)$$

where p, q refer to the two antennae. The representation of V_{pq} as a 2 x 2 matrix is equivalent to the Stokes polarisation formulation, for example in an XY basis,

$$\mathbf{V}_{pq} = \mathbf{J}_p \langle \mathbf{E}_p \mathbf{E}_q^H \rangle \mathbf{J}_q^H \quad (1.4)$$

$$= \mathbf{J}_p \begin{pmatrix} \langle E_{xp} E_{xq}^* \rangle & \langle E_{xp} E_{yq}^* \rangle \\ \langle E_{yp} E_{xq}^* \rangle & \langle E_{yp} E_{yq}^* \rangle \end{pmatrix} \mathbf{J}_q^H \quad (1.5)$$

$$= \mathbf{J}_p \begin{pmatrix} I + Q & U + iV \\ U - iV & I - Q \end{pmatrix} \mathbf{J}_q^H, \quad (1.6)$$

where I is the coherence of the total flux, V is the coherence of the circularly polarised flux, Q and U relate to coherence of the linear polarisation. Note that the Jones matrices are assumed to be constant over the averaging interval.

We now review the RIME for a single, uncorrupted, unpolarised point source, which will illustrate the Fourier transform relation between the measured visibility and a section of approximately flat sky. Considering that there are no signal corruptions (including station gains), the only Jones matrix to consider is the effect of the phase difference of the electric fields measured at the two antennae. This is due to the difference in propagation path length. Consider the vector $\boldsymbol{\sigma}$ which points from the centre of the Earth towards the source. We define the position difference between the two antenna or baseline vector $\mathbf{u} = (u, v, w)$ with the w -axis in the direction of $\boldsymbol{\sigma}$. Next we denote the angular position on the sky by (l, m) which are the directional cosines on the sky measured in the direction of (u, v) respectively. Note that we consider only a small approximately flat section of the celestial sphere centred on $\boldsymbol{\sigma}$, also called the *phase centre*. The phase difference is therefore

$$\delta\phi = 2\pi(\mathbf{u}/\lambda \cdot \boldsymbol{\sigma}) \quad (1.7)$$

Considering only a small approximately planar component of the sky (i.e. $l^2 + m^2 \ll 1$),

$$\delta\phi = 2\pi\lambda^{-1}(u_p l + v_p m). \quad (1.8)$$

Denoting the brightness matrix $\mathbf{B} = \langle \mathbf{E}_p \mathbf{E}_q^H \rangle$ and setting the delay of antenna q as the reference, the RIME for our simplified model becomes

$$\mathbf{V}_{pq} = K_p \mathbf{B} K_q^H \quad (1.9)$$

$$= \exp(2\pi i \lambda^{-1}(ul + vm)) \mathbf{B}(1) \quad (1.10)$$

where K was the Jones matrix used to apply the phase difference to each antenna. This is a Fourier Transform relation between visibility domain (u, v) and image domain (l, m) . This derivation can be easily extended

sources (e.g. see [?]). The quantity $K_p \mathbf{B} K_q^H$ is often denoted as \mathbf{X}_{pq} and is termed the coherency matrix.

An example of a Jones matrix representing a signal corruption is the complex time-variable antenna gain. Considering two independent linear dipoles, for antenna p

$$\mathbf{G}_p(t) = \begin{pmatrix} g_x(t) & 0 \\ 0 & g_y(t) \end{pmatrix} \quad (1.11)$$

Hence the RIME becomes,

$$\mathbf{V}_{pq} = \mathbf{G}_p \mathbf{X}_{pq} \mathbf{G}_q^H \quad (1.12)$$

1.1.2 A primer on self-calibration

Self-calibration, as the name suggests, uses the target itself as a calibrator to estimate station gains whilst iteratively building the sky model. In mm-VLBI calibration, self-calibration is applied under two different formulations, the first is a procedure termed *fringe fitting*. From the point of view of the RIME, fringe-fitting solves a linearised version of equation 12 for each solution interval

$$\begin{aligned} \mathbf{V}_{pq}(t_0, dt, \nu_0, d\nu) = & |G_p| |G_q| \mathbf{X}_{pq} \exp(i[\phi_p(t_0, \nu_0) + \partial_t \phi_p(t, \nu_0) dt \\ & + \partial_\nu \phi_p(t_0, \nu) d\nu - \phi_q(t_0, \nu_0) - \\ & \partial_q \phi_p(t, \nu_0) dt - \partial_\nu \phi_q(t_0, \nu) d\nu]) \end{aligned} \quad (1.13)$$

This is essentially a blind search for the station gain amplitude and phase and the first partial derivative of station phase with respect to frequency and time. The station gain amplitude will often be calibrated separately, reducing the number of parameters to solve for. The sky model used is typically just a point source at the centre of the field.

From the point of view of the RIME, self-calibration solves equation 12, However the procedure for finding sources is non-linear Naturally then, this procedures has to be given an initial sky model to start with.

iteratively, at each point adding new components to the source model. The interaction of this calibration procedure with a variable source, tropospheric, ISM and instrumental signal corruptions is of central interest to this investigation.

1.1.3 mm-VLBI observables and data products

If the visibility phase is highly variable as in the case of a turbulent atmosphere, conventional calibration and imaging techniques have severely limited (if any) success. However information can still be extracted from the raw visibilities in the form of closure quantities [29] or polarisation ratios [14]. Visibility amplitudes are also used although they suffer from systematic errors. Imaging procedures which use closure quantities as a regulariser. Closure phase, defined as the sum of 3 visibility phases of a triangle of stations $\{i, j, k\}$, is a probe of asymmetry in source structure,

$$\Phi_{ijk} = \phi_{ij} + \phi_{jk} + \phi_{ki}. \quad (1.14)$$

Because most signal corruptions are station based, the gain phase terms $\phi_{ij} = \phi^{\text{true}} + \phi_i^G - \phi_j^G$ for each antenna, assuming constant over the integration time and bandwidth will cancel, yielding a more robust observable.

In the literature, the uncertainty on the closure phase is calculated in various ways. One method is model dependent [37] and is given as a function of the SNR s of each baseline

$$u(\Phi_{ijk}) = \frac{\sqrt{4 + (s_{ij}s_{jk})^2 + (s_{jk}s_{ki})^2 + (s_{ij}s_{ki})^2 + 2(s_{ij}^2 + s_{jk}^2 + s_{ki}^2)}}{s_{ij}s_{jk}s_{ki}}, \quad (1.15)$$

where s_{ij} is defined as

$$s_{ij} = |V_{ij}| \sqrt{\frac{\tau \Delta \nu}{SEFD_i SEFD_j}}, \quad (1.16)$$

where τ is the vector averaging timescale, $\Delta \nu$ is the bandwidth, $|V_{ij}|$ is the visibility amplitude and $SEFD$ is the system equivalent flux density.

Alternatively, assuming Gaussian errors the uncertainty on the closure phase over a scan $u(\Phi_{ijk}) = \sigma(\Phi_{ijk})/\sqrt{n}$ [6].

1.1.4 Variability and the static source assumption

Implicit in our description of interferometry above (e.g. equation 9), we assumed that the source remains approximately unchanged or static during the course of the observation. However, if this assumption does not hold (i.e. if the source is time-variable), the visibilities measured over the course of an observation can no longer be related to a single image. Note that I am using

the term ‘variability’ in a general sense which refers to changes in any source observables. ‘Variability’ is most often used to denote changes in source flux but we extend the definition to include changes in source structure, position and polarisation. We expect that an image of a variable source would appear smeared out as it is averaged over many realisations and that ghosts should arise during the calibration/deconvolution procedure [citations? trienko’s papers?]. One of the objectives of this thesis will be to characterise the errors which emerge when a variable source is self-calibrated in the presence of tropospheric-induced errors. Practically it is difficult to separate source and instrumental variability without accurate models for both.

Although the static source assumption holds for most interferometric observations, the accretion flow and/or magnetic field structures around a SMBH can be variable on far shorter timescales. The primary mm-VLBI target, Sgr A*, exhibits variability on timescales of minutes to hours in the radio (including EHT observations), near-infrared (NIR), and X-ray bands [e.g. 2, 16, 42?, 13?]. This wealth of observational data has yielded several answers but the origin of the variability is still highly debated. To explain the observed delays between flares in different frequency bands, an expanding adiabatic plasma model (Marrone, 2008) has been presented however a recent flare observed with the EHT did not exhibit the increase in size expected from an expanding plasma outflow model [13]. Signatures of periodic variability at NIR and x-ray [?] have been used to argue for the presence of orbiting hotspots [10]. As the Innermost Stable Circular Orbit (ISCO) depends on spin of the BH, the spin can be constrained through the detection periodic orbital features. On the other hand, a more recent observation of a longer light curve in the NIR is more representative of a power-law scale variability [28]. The cumulative evidence of these observations point to the possibility of multiple flaring mechanisms. An important mm-VLBI observational result is that variability in the polarisation domain is far more rapid than the total intensity (Johnson 2015b), indicating that the magnetic fields structure is highly dynamic.

In principle, the variability timescale could be comparable to the period of the Innermost Stable Circular Orbit (ISCO), which for Sgr A*, ranges from 4 minutes in the case of a maximally rotating BH with a prograde disc to about half an hour for a non-rotating BH. The ISCO period for M87 is substantially longer, on the order of days. Considering light crossing times Δt_{cross} , we can estimate the angular size θ of the emission region to be of order $\theta \sim \Delta t_{\text{cross}} c / D_{\text{src}}$, where c is the speed of light and D_{src} is the observer-source distance. Hence for Sgr A* at $D_{\text{src}} = 8.3$ kpc (Gillessen, 2009), a flare of duration $\Delta t_{\text{cross}} = 10$ min corresponds to scales of $15 R_{\text{Sch}}$. Such analyses

gave early evidence for an emission area on event horizon scales.

In the case of a highly localised flare, several approaches [10?, 21] show that EHT can track such a structure with $\sim 5 \mu\text{-arcsec}$ precision using closure quantities and polarimetric ratios. This could help map the spacetime around the BH. Alternatively (author?) [25] show that a gaussian weighting scheme can be applied to mitigate the effects of variability and measure the quiescent structure although this approach would downweight the longest baselines. However all of these approaches assume only gaussian thermal noise, gaussian-blurring in the ISM and no tropospheric-induced calibration errors.

1.2 Signal Corruptions

We begin with an introduction to scattering theory, which is applicable to the radiative processes occurring in both the troposphere and ISM. Following this we explore signal corruptions due to the transmission through the ISM and Earth’s atmosphere as well as instrumental imperfections in detail.

1.2.1 Scattering basics

Millimetre wavelength radiation originating at the Galactic Centre is repeatedly scattered along the signal path to the Earth-based observer. The first occurrence is due to electron plasma in the ISM [e.g. 5, 19], while the second is due to poorly-mixed water vapour in the Earth’s troposphere [e.g. 7, 23]. It is essential that the effects of the scattering phenomena are understood for accurate calibration and robust inference of the intrinsic source properties. To this end, simulation modules approximating scattering in both media are implemented in MEQSILHOUETTE. As an introduction to the separate descriptions of each, we review a simple scattering model.

An electro-magnetic wave is scattered when it passes through a medium with refractive index inhomogeneities. Following (author?) [30], this effect can be modeled as a thin screen, located between source and observer planes and orientated perpendicular to the line-of-sight. The screen, indexed by coordinate vector \mathbf{x} , adds a stochastic phase $\phi(\mathbf{x})$ to the incoming wave at each point on the screen, yielding a corrugated, outgoing wavefront. We define the Fresnel scale as $r_F = \sqrt{\lambda D_{\text{os}}/2\pi}$, where D_{os} is the observer-scatterer distance, or the distance where the geometrical path difference $\frac{2\pi}{\lambda}(D_{\text{os}} - \sqrt{D_{\text{os}}^2 + r_F^2}) = \frac{1}{2} \text{ rad}$.

To determine the resultant electric field at a point in the plane of the

observer, indexed by coordinate vector \mathbf{X} , one has to take into account all possible ray paths from the screen to \mathbf{X} . To illustrate the model, a calculation of the scalar electric field generated by a point source, $\psi(\mathbf{X})$ yields the Fresnel-Kirchoff integral [3]

$$\psi(\mathbf{X}) = C \int_{\text{screen}} \exp \left[i\phi(\mathbf{x}) + i \frac{(\mathbf{x} - \mathbf{X})^2}{2r_F} \right] d\mathbf{x}, \quad (1.17)$$

where C is a numerical constant.

The statistical properties of $\phi(\mathbf{x})$ can be described by a power spectrum or equivalently the phase structure function,

$$D_\phi(\mathbf{x}, \mathbf{x}') = \langle [\phi(\mathbf{x} + \mathbf{x}') - \phi(\mathbf{x})]^2 \rangle, \quad (1.18)$$

where \mathbf{x} and \mathbf{x}' represent two points on the screen and $\langle \dots \rangle$ denotes the ensemble average.

There is evidence that D_ϕ can be reasonably approximated by a power law dependence on the absolute distance r between points on the screen [1?]

$$D_\phi(r) = (r/r_0)^\beta, \quad r^2 = (\mathbf{x} - \mathbf{x}')^2 \quad (1.19)$$

where r_0 is the phase coherence length scale defined such that $D_\phi(r_0) = 1$ rad. Kolmogorov turbulence, which describes how kinetic energy injected at an outer length scale r_{out} cascades to increasingly smaller scales until finally dissipated at an inner length scale r_{in} , predicts $\beta = 5/3$ in the domain $r_{\text{in}} \ll r \ll r_{\text{out}}$. This scaling has been demonstrated to be a reasonable approximation for the ISM over scales $r \sim 10^2$ km to > 1 AU [?], and also for the troposphere with $r < \Delta h$, where Δh is the thickness of the turbulent layer [8]. The specifics of the tropospheric model will be explored further in later sections.

The two length scales, r_F and r_0 , define the nature of the scattering which is split into the strong and weak regimes, Fig. 1. In weak scattering, $r_0 \gg r_F$ and hence by equation 19, $D_\phi(r_F) \ll 1$. This implies that most of the radiative power measured on a point \mathbf{X} will originate from a screen area $A_{\text{weak}} \approx \pi r_F^2$. Whereas in the regime of *strong scattering*, $r_0 \ll r_F$ yielding $D_\phi(r_F) \gg 1$. This results in coherent signal propagation onto the point \mathbf{X} from multiple disconnected zones each of area $A_{\text{strong}} \approx \pi r_0^2$ [30]. Scattering in the troposphere and ISM in the direction of the Galactic Centre fall into the regimes of weak and strong scattering respectively.

To evolve the screen in time, we assume a frozen screen i.e. that the velocity of the individual turbulent eddies is dominated by the bulk motion

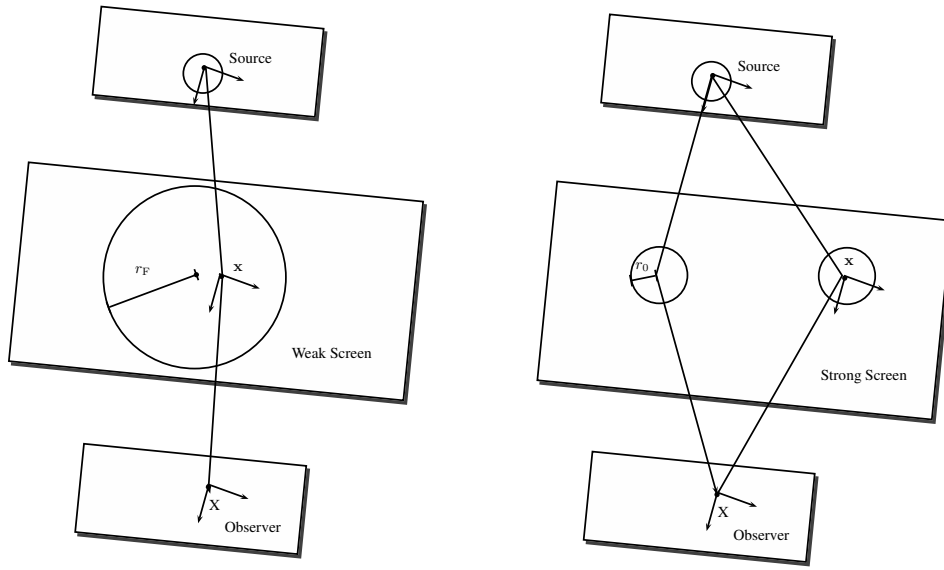


Figure 1.1: Illustration depicting the basics of scattering in the weak (left) and strong (right) regimes. In the weak regime, the signal is coherently propagated over an area, $A_{\text{weak}} \approx \pi r_F^2$ whereas in the strong regime, coherent propagation is split over many areas of size $A_{\text{strong}} \approx \pi r_0^2$.

of scattering medium [e.g. 23]. This allows us to treat the screen as frozen but advected over the observer by a constant motion. Hence time variability can be easily incorporated by the relative motion between source, scattering screen and observer.

1.2.2 Interstellar medium scattering

Electron density inhomogeneities in the interstellar medium (ISM) plasma scatter the radio emission from the Galactic centre. Radio interferometric observations of Sgr A* have characterised the basic properties of the intervening plasma material, however extensive developments in scattering theory and simulations have proved essential to the interpretation of more subtle scattering phenomena. This section begins with the early observational results which studied the Gaussian blurring effect of the scattering; we then expand on the scattering theory introduced in Sec. 2.1 to review the latest theoretical developments which explore the presence of scattering-induced substructure; finally we review recent observational results which account for scattering substructure in their data interpretation.

The dominant observational effect of the scattering for $\lambda \gtrsim \text{cm}$ is to convolve the intrinsic source structure with an elliptical Gaussian. The size of the Gaussian exhibits a λ^2 scaling dependence over several orders of magnitude [Fig. 2 ? 38, 5, 24], which is consistent with the wavelength dependence of the refractive index of a plasma. In order to determine the parameters of the scattering kernel, i.e. major axis, minor axis and position angle, one has to observe at wavelengths where the angular size of scattering ellipse is much larger than the expected source size. A Very Long Baseline Array (VLBA) + Green Bank Telescope (GBT) campaign [5] estimated the size at $1.31 \times 0.64 \text{ mas cm}^{-2}$, oriented 78° east of north.

An accurate extrapolation of scattering kernel to 1.3 mm is important for the EHT scattering-mitigation strategy [15] which aims to deblur the scattered image through a deconvolution procedure. However as this extrapolation is over at least an order of magnitude, any small systematic error in the original measurement can significantly effect the 1.3 mm extrapolated parameters. A recent review of VLBI observations of Sgr A* [35] has noted that there are significant inconsistencies between different measurements. The authors used a Bayesian methodology to re-analyse the datasets resulting in increased uncertainties as shown in 1. The minor axis has a much larger uncertainty than the major axis due to the limited north-south coverage of the VLBA.

The Gaussian blurring effect can explained by the simple scattering

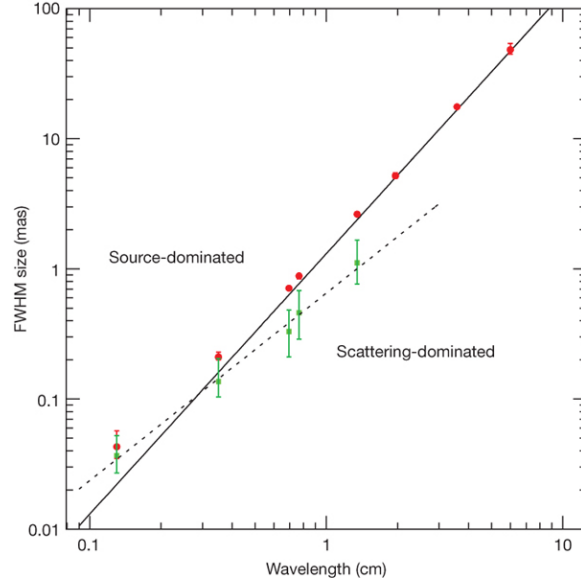


Figure 1.2: The λ^2 dependence of scattering kernel size is shown by the solid line. This has been derived from measurements made at $\lambda > 17$ cm [5]. The dotted line shows the derived intrinsic source size which scales as $\lambda^{1.44}$. This was derived from measurements in the wavelength range, $2 \text{ cm} < \lambda < 1.3 \text{ mm}$. The red circles show major-axis observed sizes of Sgr A* and the green points show the derived intrinsic major-axis size. This plot was reproduced from (author?) [12].

Table 1.1: A re-analysis of VLBI observations of Sgr A* by (author?) [35] has yielded revised estimates of the parameters associated with the Gaussian scattering kernel. An accurate estimation is needed for accurate extrapolation to 1.3 mm. Note that the position angle is measured East of North.

major axis FWHM (mas/cm ⁻²)	1.32	0.04
minor axis FWHM (mas/cm ⁻²)	0.82	0.21
position angle (°)	77.8	9.7

model introduced in Sec. 2.1. Recall, that in the strong scattering regime light is propagated from coherent patches with linear size $\sim r_0$. Each patch will emit light coherently into a single-slit diffraction cone of angular size $\theta_{\text{scatt}} \sim \lambda/r_0$. An observer will hence be illuminated by many patches spanning θ_{scatt} , yielding a blurred and broadened image, with projected size on the screen equal to the *refractive scale*

$$r_{\text{ref}} = \theta_{\text{scatt}} D_{\text{os}} = r_{\text{F}}^2/r_0.$$

r_{ref} is the third fundamental length scale in the strong scattering regime and is associated with the refractive timescale,

$$t_{\text{ref}} = r_{\text{ref}}/v.$$

We can calculate r_0 given the FWHM of θ_{scatt} through the more precise relation

$$\theta_{\text{scatt}} = \frac{2\sqrt{2\ln 2}}{2\pi} \lambda/r_0(M+1) \quad (1.20)$$

where $M = D_{\text{os}}/R$ is the magnification and R is the source-screen distance. The magnification factor is a correction to the model introduced in Sec. 2.1 when $R \sim \infty$ no longer holds and should be used when calculating distances in the observer plane [17]. The location of the scattering medium was originally thought to be quite close to Sgr A*. However, observations of a newly discovered pulsar, SGR J1745-29, indicate that the scattering screen is located at a distance $D_{\text{os}} = 5.8 \pm 0.3$ kpc, within the Scutum spiral arm. Using Eq. 20 and the parameters given in table 1, we find that the major axis of the coherence length at 1.3 mm, $r_0 \approx 3136.67$ km.

As the VLBI moves to higher frequencies, focus has shifted away from the well-studied Gaussian convolution effect of ISM scattering and onto the presence of stochastic scattering-induced substructure. To understand this phenomenon, we must first develop our conceptual framework.

Strong scattering can be further subdivided into *snapshot*, *average* and *ensemble-average* regimes [31, 17]. To understand the different regimes, remember that for each point on the source, the observer sees emission from coherent patches of size $\sim r_0$ spanning $\sim r_{\text{ref}}$. The diffraction cones from each of the patches will interfere, resulting in a multi-slit *diffractive scintillation* pattern.

In the *snapshot regime*, a compact source is observed with a narrow bandwidth and over a short time integration. This yields a single realisation of the diffractive scintillation pattern. By averaging over many snapshots, diffractive scintillation is quenched. This occurs if the source size θ_{src} is much larger

than the diffractive scale $\theta_{\text{src}} \gg r_0/R$; if the fractional bandwidth $\delta\nu/\nu$ is much larger than the decorrelation bandwidth $\delta\nu/\nu \gg \delta\nu_{\text{dc}}/\nu \approx (r_0/r_{\text{F}})^2$ [30]; or if the integration time t_{int} is much larger the diffractive timescale $t_{\text{int}} \gg t_0 = r_0/v$, where v is the relative velocity between screen, source and observer. This regime is hence only accessible through observations of compact objects like pulsars. On a side note, observations in this regime can be used to probe the source with angular resolution given by the $\sim \lambda/r_{\text{ref}}$ [e.g. 18]. This is because the scattering screen is essentially a lens of size $\approx r_{\text{ref}}$.

In the *average regime*, diffractive scintillation has been averaged over, however there still exists scintillation over scales comparable to the size of the scattered image of a point source $\sim r_{\text{ref}}$, termed *refractive scintillation*. Phase fluctuations on this scale acts like a weak lens to focus or defocus the λ/r_0 scale diffraction cones in the direction of the observer. For a point source this would lead to weak flux variations in the total flux [30]. We will show later that refractive scintillation leads to the presence of sub-structure for a resolved scatter-broadened source. In contrast to diffractive scintillation, refractive scintillation is much more difficult to average over. Typically the refractive time scale $t_{\text{ref}} = r_{\text{ref}}/v$ is on the order of weeks to months for Sgr A^{*}; the fractional decorrelation bandwidth is on the order of unity $\delta\nu_{\text{dc}}/\nu \sim 1$; and the source has to be much larger than the image of a scattered point source $\theta_{\text{src}} \gg \theta_{\text{scatt}}$.

In the *ensemble-average regime*, both diffractive and refractive scintillation have been averaged over. It is in this regime when the scattering is equivalent to Gaussian convolution which is deterministic and not time variable.

A recent theoretical work [?] has derived a useful approximation of the resolved scattered image I_{ss} in the average regime,

$$I_{\text{ss}}(\mathbf{x}) \approx I_{\text{src}}(\mathbf{x} + r_{\text{F}}^2 \nabla \phi(\mathbf{x})), \quad (1.21)$$

where ∇ is the directional derivative. Here we have used the same two-dimensional coordinate system, indexed by \mathbf{x} to describe the source, screen and observer planes which are considered to be aligned along the vertical axis. The scattered image I_{ss} is approximated by a 'reshuffling' of the source image I_{src} . As $|\nabla \phi| \sim 1/r_0$, the magnitude of the translation of points on $I_{\text{src}} \sim r_{\text{ref}} \sim 10 \mu\text{-arcsec}$ in the case of Sgr A^{*}.

Even though $\phi(\mathbf{x})$ is only coherent to $\sim r_0$, the directional phase derivative $\nabla \phi(\mathbf{x})$ remains spatially coherent over much larger scales. Following [?], the autocovariance of phase derivative can be related to the structure

function

$$\langle [\partial_x \phi(\mathbf{x}_0)] [\partial_x \phi(\mathbf{x}_0 + \mathbf{x})] \rangle = -\partial_x^2 \langle \phi(\mathbf{x}_0) \phi(\mathbf{x}_0 + \mathbf{x}) \rangle \quad (1.22)$$

$$= \partial_x^2 D_\phi(\mathbf{x}). \quad (1.23)$$

as $\langle \phi(\mathbf{x})^2 \rangle = 0$

Using a typical structure function [?], We are interested in the case $r_{\text{in}} \gg r_0$, the structure function becomes [?]

$$D_\phi = \begin{cases} \left(\frac{r}{r_0}\right)^2 & \text{if } r \ll r_{\text{in}}, \\ \frac{2}{\beta} \left(\frac{r_{\text{in}}}{r_0}\right)^{2-\beta} \left(\frac{r}{r_0}\right)^\beta & \text{if } r \gg r_{\text{in}}. \end{cases}$$

Note that the structure function is quadratic at small scales as fluctuations are smooth and then kolmogorov then constant (Tatarskii, 1971). Hence We are interested in the case r/ggr_{in}

$$\partial_x^2 D_\phi(\mathbf{x}) = \left(\frac{r_{\text{in}}}{r_0}\right)^{2-\beta} 2(\beta-1) \frac{r^{\beta-2}}{r_0^\beta} \quad (1.24)$$

Therefore in the Kolmogorov regime $\beta = 5/3$, the coherence of image shift relative to the refractive scale $\propto (r/r_0)^{-1/3}$. Inner scale extends coherence and outer scale cuts it off.

Even though $\phi(\mathbf{x})$ is only coherent to $\sim r_0$, $\nabla \phi(\mathbf{x})$ remains spatially coherent over much larger scales, leading to the presence of refractive substructure [?].

A recent observation of Sgr A* at 3.5 mm by the VLBA+LMT [see Fig. reffig:substructure2 ?] show that the closure phase measured is consistent with refractive scintillation. Another observation at 1.3 cm shows flux modulation due to scattering substructure ~ 10 mJy [19] and other predictions show ~ 60 mJy for long East-West baselines and ~ 25 mJy for long North-South baselines [?], assuming a Gaussian source of $FWHM = 40 \mu\text{-arcsec}$.

Distinguishing intrinsic source structure and variability and ISM variability is an interesting challenge. Observations at mm-wavelengths have revealed deviations from the λ^2 scattering scaling law, see Fig. 2. This is interpreted as due to the presence of intrinsic source structure and has been fitted with a power-law with an exponent of 1.34 ± 0.01 [24]. This has enabled the constraint of various theoretical models [5], excluding advection-dominated accretion flows (ADAF) [?] and Bondi-Hoyle accretion [?].

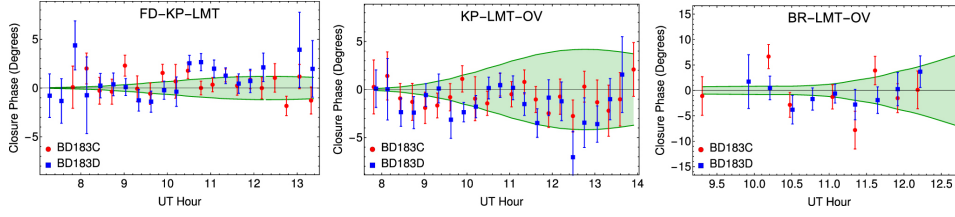


Figure 1.3: Closure phases recorded in a VLBA + LMT observation of Sgr A* at $\lambda = 3.5$ mm [?]. The data points are shown as red circles and blue squares and are only distinguished by the calibrator used. The green envelopes show the 1σ closure phase prediction induced by scattering-induced substructure. Reproduced from [?].

However observations extending over month timescales are required to properly sample the larger scale inhomogeneities and even with multiple epoch observations, it can be difficult to distinguish source and scattering characteristics [26].

Knowledge of the scattering characteristics can allow the two to be decoupled without sampling a refractive ensemble. It therefore provides a robust and rapid mechanism for quantifying refractive effects.

1.2.3 Troposphere

The coherence and intensity of millimetre wavelength electromagnetic waves are most severely deteriorated in the lowest atmospheric layer, the troposphere which extends up to an altitude of 7 – 10 km above sea level and down to a temperature $T \sim 218$ K [39]. The troposphere is composed of a number of different components including primary gases N_2 and O_2 , trace gases e.g. water vapour and CO_2 , as well as particulates of water droplets and dust. The rest of this section will explore the tropospheric corruption for the mm-VLBI case.

Propagation fundamentals

Consider a quasi-monochromatic wave passing through a linear medium,

$$E_\nu(x, t) = E_0 \exp^{i(kn_\nu x - 2\pi\nu t)}, \quad (1.25)$$

where $k = 2\pi\nu/c$ is the propagation constant in free space and $n = n_R + jn_I$ is the complex index of refraction. Note that we will occasionally omit the

frequency dependence of n and related quantities to simplify the notation. If n_I is nonzero, the electric flux I will decay exponentially

$$I = EE^* = E_0^2 \exp(-\tau), \quad (1.26)$$

where τ is called the opacity or optical depth and is related to the absorption coefficient, $d\tau = \kappa dx$ where $\kappa = 4\pi\nu n_I/c$. If $n_R > 1$ the phase velocity of light will decrease, $v_p = c/n_R$, which results in a time delay. The time delay due to the troposphere, \tilde{t} and opacity τ can be calculated simultaneously,

$$\tilde{t} + i\tau/4\pi\nu = 1/c \int_{path} d\mathbf{s} (n_\nu(\mathbf{s}) - 1). \quad (1.27)$$

In the interferometric context opacity and time delay are often viewed independently. However, the electric field is real and causal which imposes restrictions on the complex refractive index. Specifically n_R and n_I contain the same information and can be interchanged via the Kramers-Kronig relations.

Absorption is accompanied by emission and for a medium in local thermodynamic equilibrium, Kirchoff's law states that

$$\frac{\epsilon_\nu}{\kappa_\nu} = B_\nu(T), \quad (1.28)$$

where $\epsilon_\nu = dI_\nu/dx$ is the emission coefficient and $B_\nu(T)$ is the Planck function. Hence the absorbing molecules are also emitters, increasing system noise. Therefore opacity, time delay and atmospheric noise are interrelated and should be simulated consistently. On a side note these relations allow for phase calibration using measurements of sky emission via Water Vapour Radiometry (WVR) [e.g. 7].

Atmospheric corruptions in the (sub-)mm regime

An analysis of the absorption spectrum in the GHz range (Fig. 4), shows that it is dominated by transitions of H_2O and O_2 as well as a pseudo-continuum opacity which increases with frequency. The pseudo-continuum opacity is due to the cumulative effect of the far wings of a multitude of broadened water vapour lines above 1 THz [7]. At 230 GHz the absorption is typically 5 – 10% at the best sites, during good weather.

In contrast to the dry atmospheric components, water vapour mixes poorly and its time-variable spatial distribution induces rapid fluctuations

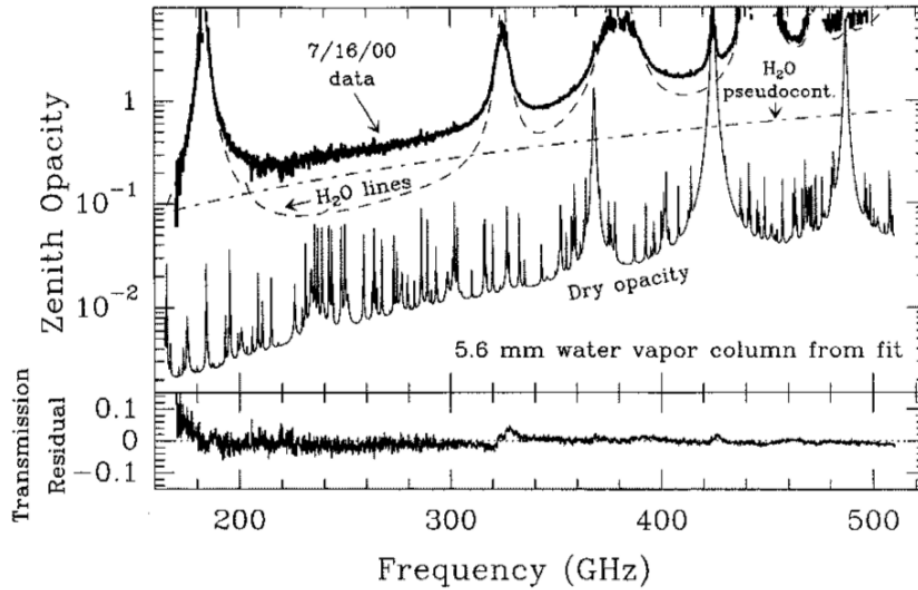


Figure 1.4: Recorded zenith absorption spectrum in the 160 – 520 GHz range, taken on Mauna Kea at an altitude of ~ 4000 m. The data has been fit to a sum of H₂O lines, an H₂O pseudo-continuum and dry absorption lines. The model has been generated using the ATM code, with the bottom panel showing the residuals. Here 'dry' refers to all atmospheric constituents except H₂O. Reproduced from (author?) [33]

in the time delays \tilde{t} above each station. The phase error for a baseline (1,2) where antenna 1 is the reference will be

$$\delta\phi(t, \nu) = (\tilde{t}_2(t, \nu) - \tilde{t}_1(t, \nu))/\nu. \quad (1.29)$$

The water vapour column density is measured as the depth of the column when converted to the liquid phase and is referred to as the precipitable water vapour (PWV). PWV is directly proportional to the time delay and hence the phase delay,

$$\delta\phi \approx \frac{12.6\pi}{\lambda} \times w, \quad (1.30)$$

where w is the depth of the PWV column [7] and an atmospheric temperature $T = 270$ K has been assumed. This relationship between phase and water vapour content has been experimentally verified [20]. At 230 GHz, the change in PWV needed to offset the phase by 1 rad is $\Delta w \approx 0.03$ mm.

This sensitive dependence of phase coherence on atmospheric stability is aggravated by typically low antenna observation elevation angles as the atmospheric path length is increased; uncorrelated atmospheric variations between stations as correlated atmospheric variations fall away; and observing with a sparse VLBI array as this leads to less redundancy for calibration.

Radiative transfer

The problem of radiative transfer through the Earth's atmosphere is well described and implemented by the Atmospheric Transmission at Microwaves (ATM) description and code [33]. In this section we provide a brief summary of the theory underpinning the package and we encourage the reader to see the original paper for further detail. The incorporation of ATM into the MEQSILHOUETTE simulator is dealt with in section 4.2. ATM is commonly used in the Atacama Large Millimeter Array (ALMA) community [9, 32] and has been tested with atmospheric transmission spectra taken on Mauna Kea [?].

We start from the unpolarised radiative transfer equation, which is unidirectional in the absence of scattering,

$$\frac{dI_\nu(s)}{ds} = \epsilon_\nu(s) - \kappa_\nu(s)I_\nu(s), \quad (1.31)$$

where s is the coordinate along the signal path through the atmosphere. The assumption of local thermodynamic equilibrium (LTE) holds as the collisional timescale is much smaller than the time for spontaneous emission

up to altitudes ≥ 80 km, after which there is only $\sim 0.001\%$ of mass left [33]. Applying 28, multiplying by $\exp(-\tau_\nu)$ and integrating from the top of the atmosphere ($s = 0$) yields,

$$I_\nu(s) = I_\nu(0)e^{-\tau_\nu(0,s)} + \int_0^s B_\nu(s')e^{-\tau_\nu(s',s)}\kappa_\nu(s')ds', \quad (1.32)$$

where s' is a dummy variable in the same direction as s and $\tau_\nu(0,s) = \int_0^s \kappa_\nu(s')ds'$. $I_\nu(0)$ is normally taken as the radiance from the cosmic background. 32 will allow us to calculate the noise temperature of the atmosphere by converting the output radiance at the ground $I_\nu(s)$ to the equivalent blackbody temperature through inversion the Planck function. To calculate the opacity and complete the above integral, κ_ν needs to be calculated over the frequency range. The time delay \hat{t} can be calculated using the Kramers-Kronig relations.

A general equation for the absorption coefficient for a transition between a lower l and upper u states is given in the original paper. Here we merely point out that it should be proportional to the energy of the photon, $h\nu_{l \rightarrow u}$, the transition probability or Einstein coefficient, $B_{l \rightarrow u}$, the line-shape, $f(\nu, \nu_{l \rightarrow u})$ and the number densities N of electronic populations. Line profiles which describe pressure broadening (perturbations to the Hamiltonian due to the presence of nearby molecules) and Doppler broadening are used. The condition of detailed balance further requires that decays from the upper state are included yielding, $g_u B_{u \rightarrow l} = g_l B_{l \rightarrow u}$, where g is the degeneracy of the electronic state. Putting this together we find,

$$\kappa(\nu)_{l \rightarrow u} \propto h\nu B_{l \rightarrow u} \left(\frac{N_l}{g_l} - \frac{N_u}{g_u} \right) f(\nu, \nu_{l \rightarrow u}), \quad (1.33)$$

where the Einstein coefficients are calculated from the inner product of the initial and final states with the dipole transition operator,

$$B_{l \rightarrow u} = \frac{2\pi}{3\hbar^2} |\langle u | \mu | l \rangle|^2, \quad (1.34)$$

where $|u\rangle$, $|l\rangle$, $|\mu\rangle$ are the wavefunctions of upper and lower states and the dipole transition operator respectively. The number densities of the two states, N_u and N_l in local thermodynamic equilibrium (LTE) are simply related to the local number density and temperature via Boltzmann statistics,

$$\frac{N_n}{N} = g_n \frac{\exp -\frac{E_n}{kT}}{Q} \quad (1.35)$$

where Q is the partition function. $Q = \sum_i g_i \exp -E_n/kT$.

Physically, the lineshape originates from perturbations to the hamiltonian due to proximity to neighbouring molecules, called pressure broadening, and at lower pressures, thermal doppler broadening. A Van Vleck - Weisskopf (VW) profile is used for pressure broadening. At lower pressures this is convolved with a Gaussian which arises from the Maxwellian distribution. Far wing broadening of H_2O lines > 1.2 THz extends to lower frequencies and is not completely represented by the VW profile. This is believed to be due to self-self collisions of water molecules. Additionally there are terms from the dry atmosphere related to transient dipoles and Debye absorption which are not represented in the lineshape. To correct for these effects two pseudocontinua are used, which take the form of a power law dependence on frequency, temperature and the molecular densities.

Transition lines at radio wavelengths result from rotational state transitions. To calculate the inner product given in equation 34, hamiltonians for linearly symmetric rotors (e.g. O_2 , CO) and asymmetric rotors are used. The asymmetric rotations are decomposed into three principal rotation axes with differing rotational constants governing each axis. Rotational constants were measured by the authors as well as drawn from a variety of literature. Partition functions and transition probability are calculated using approximations taken from the literature.

Turbulent phase fluctuations

Visibility phase instability $\delta\phi(t)$ due to tropospheric turbulence is a fundamental limitation to producing high fidelity, science-quality maps with a mm-VLBI array [39]. The coherence time-scale is typically too rapid ($\lesssim 10$ s) for fast switching calibration, so other calibration procedures (e.g. water vapour radiometry, paired antennas, and/or self-calibration) must be performed. Self-calibration is the most commonly used but is limited by the integration time needed to obtain adequate SNR to fringe fit. Phase decoherence often leads to the use of closure quantities to perform model fitting [11, 4, 38], and causes a decrease in measured flux due to incoherent complex averaging. In the section we will review and develop the weak scattering theory introduced earlier which will culminate in a formulation for the simulation of tropospheric phase turbulence seen by a mm-VLBI array. How this formulation is implemented and fits into the broader atmospheric simulation framework will be discussed in section 4.2.

Following from section 2.1, we can model the statistics of $\delta\phi(t)$ with a thin, frozen, Kolomogorov-turbulent phase screen moving with a bulk

velocity, v . We set the height h of the screen at the water vapour scale height of 2 km above ground. We will show later that the thickness Δh of the atmospheric turbulent layer can be neglected in our implementation. At 1.3 mm, the Fresnel scale is $r_F \approx 0.45$ m and experiments show annual variations of $r_0 \sim 50 - 500$ m above Mauna Kea [27] and $r_0 \sim 90 - 700$ m above Chajnantor [36], where both sites are considered to have excellent atmospheric conditions for millimetre astronomy. As $r_F < r_0$, this is an example of weak scattering.

The required field-of-view (FoV) of a global mm-VLBI array is typically $\text{FoV} < 1$ mas or $\sim 10 \mu\text{m}$ at a height of 2 km, which is roughly 7-8 orders of magnitude smaller than the tropospheric coherence length. The tropospheric corruption can therefore be considered constant across the FoV and, from the perspective of the Measurement Equation, modeled as a diagonal Jones matrix per time and frequency interval. As VLBI baselines are much longer than the coherence length, $|\mathbf{b}| \geq 1000 \text{ km} \gg r_0$, the phase screen at each site must be simulated independently. This assumption only holds for VLBI baselines and the framework needs to be extended to simulate the effects of turbulence on individual phased arrays stations (e.g. SMA) and short (< 10 km) baselines (e.g. JCMT - SMA).

Our aim then is to produce a phase error time sequence $\{\delta\phi(t_i)\}$ for each station which is added to the visibility phase. We invoke the frozen screen assumption and write the structure function as a function of time, $D(t) = D(r)|_{r=vt}$. The temporal structure function $D(t)$ provides an efficient route to sample the variability of the troposphere at the typical integration time of the dataset, $t_{\text{int}} \sim 1$ sec.

The temporal variance of the phase is a function of the temporal structure function, and accounting for time integration yields [see 40, B3]

$$\sigma_\phi^2(t_{\text{int}}) = (1/t_{\text{int}})^2 \int_0^{t_{\text{int}}} (t_{\text{int}} - t) D_\phi(t) dt. \quad (1.36)$$

Assuming power-law turbulence and integrating yields,

$$\sigma_\phi^2(t_{\text{int}}) = \left[\frac{1}{\sin \theta (\beta^2 + 3\beta + 2)} \right] \left(\frac{t_{\text{int}}}{t_0} \right)^\beta, \quad (1.37)$$

where $t_0 = r_0/v$ is the coherence time when observing at zenith and $1/\sin \theta$ is the approximate airmass which arises as $D_\phi \propto w$. As $r \ll \Delta h$, where Δh is the thickness of the turbulent layer, a thin screen exponent of $\beta = 5/3$ is justified [40]. The phase error time-series takes the form of a Gaussian random walk per antenna. At mm-wavelengths, the spectrum of water vapour

is non-dispersive up to a few percent [9] and so we can assume a simple linear scaling across the bandwidth.

Phase fluctuations $\delta\phi(t)$ can also be simulated by taking the inverse Fourier transform of the spatial phase power spectrum. However this approach is much more computationally expensive, e.g. for an observation length t_{obs} involving $N_{\text{ant}} = 8$ independent antennae with dish radii $r_{\text{dish}} = 15$ m, wind speed $v = 10$ m s⁻¹ and pixel size equal to r_{F} , the number of pixels $N_{\text{pix}} \approx N_{\text{ant}} t_{\text{obs}} r_{\text{dish}}^2 / (v r_{\text{F}}^3) \sim 10^8$. Additionally, due to fractal nature of ideal Kolmogorov turbulence, the power spectrum becomes unbounded as the wavenumber approaches zero which makes it difficult to determine the sampling interval of the spatial power spectrum [22].

1.2.4 Instrumental

Thermal Noise

The level of thermal noise in the data will define the sensitivity of the interferometer to detect a source and also to distinguish fine source characteristics. Closure quantities are especially prone to high levels of thermal as several visibilities are multiplied. A derivation of the thermal noise of an interferometer can be made through derivation of the thermal noise of an antenna and then correlating the result [41]. The RMS thermal noise of an interferometer $\{i, j\}$ over a bandwidth $\Delta\nu$ and an integration time is given by

$$\Delta S_{ij} = \frac{1}{\eta_s} \sqrt{\frac{SEFD_i SEFD_j}{2\Delta\nu t_{\text{int}}}}, \quad (1.38)$$

where η_s is the system efficiency and $2\Delta\nu t_{\text{int}}$ is the number of independent samples. The *SEFD* is a measure of the sensitivity of an antenna, accounting for the efficiency, collecting area and thermal noise and is defined as the flux density of a source with the same power,

$$SEFD = 2k_{\text{B}} T_{\text{sys}} / (\eta_{\text{a}} A), \quad (1.39)$$

where A is the antenna area, η_{a} is the antenna efficiency, T_{sys} is the system temperature and the factor $\frac{1}{2}$ accounts for only sampling 1 polarisation.

Antenna Pointing

All antennas suffer pointing errors to some degree due to a variety of factors including dish flexure due to gravity, wind and thermal loading, as well

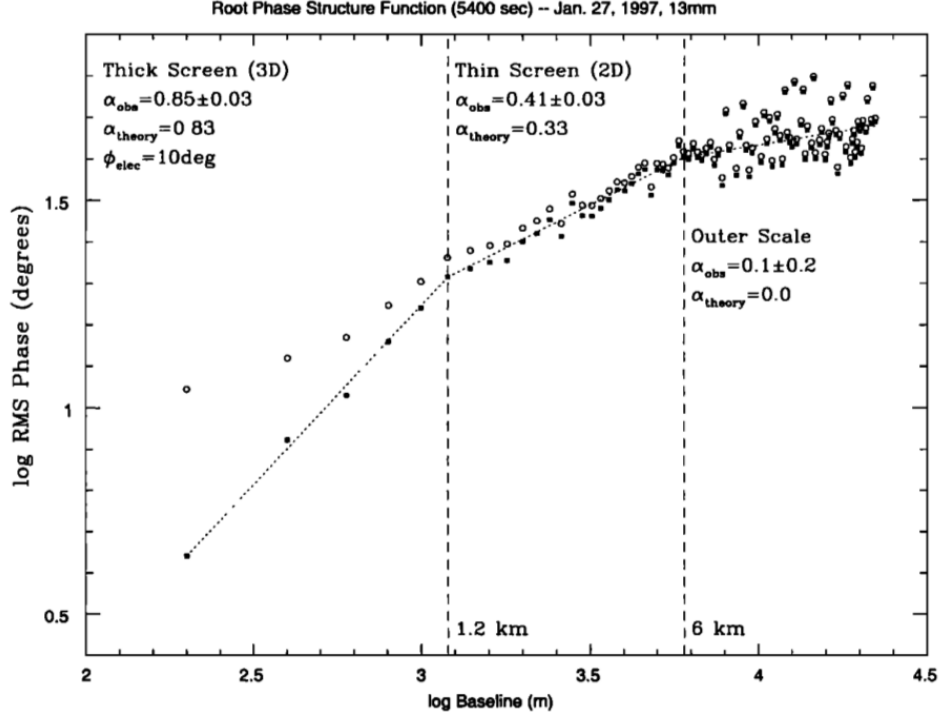


Figure 1.5: A log-log plot of RMS visibility phase versus baseline length for an observation of 1 Jy source 0748 + 240 with VLA at 22 GHz over a 90 min duration. The open circles show RMS phase as measured whereas the solid squares show the same values with a constant thermal noise contribution of 10° subtracted in quadrature. Note that the measured and theoretical Kolmogorov turbulent exponent β changes with distance on the phase screen as the viewing configuration transitions from a thick screen ($\beta_{\text{theory}} = 5/3$) to a thin screen ($\beta_{\text{theory}} = 2/3$) at $r \approx 1.2$ km and from a thin screen to completely uncorrelated regime ($\beta = 0$) beyond the outer scale at $r \approx 6$ km. Although these regimes appear distinct, there is continuous variation between them. Reproduced from ?]

as drive mechanics. This corresponds to an offset primary beam, which should only translate to minor amplitude errors if the pointing error θ_{PE} is significantly smaller than the primary beam (i.e. $\theta_{\text{PE}} \ll \theta_{\text{PB}}$). In the Measurement Equation formalism, this offset can be represented by a modified (shifted) primary beam pattern in the E -Jones term

$$\mathbf{E}_p(l, m) = \mathbf{E}(l_0 + \delta l_p, m_0 + \delta m_p), \quad (1.40)$$

where $\delta l_p, \delta m_p$ correspond to the directional cosine offsets. This could be a problem for millimetre observations as the primary beam is significant, e.g. for a 30 m dish at 1.3 mm, $\theta_{\text{PB}} \sim 10$ arcsec, compared to the pointing error which is on the order of arcseconds.

We identify two main classes of pointing error. Firstly an antenna tracking a source will suffer a slow, continuous time-variable pointing error associated with the tracking error σ_{track} . Physically this could be attributed to changes in wind, thermal and gravitational loading which all change with telescope pointing direction and over the course of a typical few hour observation. Using the MeqTrees software package, such behaviour has been demonstrated to occur with the Westerbork Synthesis Radio Telescope (WSRT, [?])¹.

Secondly, whilst a stationary phase centre is tracked, the pointing error should evolve slowly and smoothly, however, in mm-VLBI observations the phase centre is often shifted to another source/calibrator. This would cause the pointing error to change abruptly, with an absolute pointing error $\sim \sigma_{\text{abs}}$. Source/calibrator change is scheduled every 5-10 minutes in a typical millimetre observation. The point is that even though EHT will be able to determine the pointing offset when observing a calibrator with well known structure, when the antennas slew back to a source (e.g. Sgr A*) with less certain or variable source structure, the pointing error could change significantly. This is exacerbated by the scarcity of mm-wavelength calibrators, which are often widely separated from the source.

¹See also <https://indico.skatelescope.org/event/171/session/9/contribution/20>

Chapter 2

Software implementation

2.1 Design objectives

Our primary aim is to test and research mm-VLBI calibration, imaging and parameter estimation algorithms/strategies through the construction of a synthetic data simulation framework. To address the many questions within the wide scope of this objective, one must be able to setup and run a diversity of experiments within the simulation framework. This places definite constraints on the software architecture. In particular, the framework should

- enable the implementation of all relevant classes of signal corruption within a formalism which ensures consistency with the causal signal transmission chain,
- be compatible with time-variable GRMHD source models which are to be used as inputs,
- be organised in modularised structure so that it is flexible, extendable and could be incorporated by other interferometric algorithms e.g. a calibration or a parameter estimation algorithm,
- The modular structure should also enable the construction and execution of arbitrary observations.

2.2 Architecture and Workflow

In this section, we will review how the architectural design and workflow of the simulator architecture has been designed to meet the above objec-

tives. To fulfill the first objective, we try to cast signal corruptions in the RIME formalism (see section 1.1), and where this is not possible, to fit those particular signal corruptions into the casually correct position in the signal transmission chain, with proper consideration given to non-commutativity of elements in the signal transmission path. The implementation of each signal corruption is described in the following subsections. The remaining objectives fall into the realm of software design and will be discussed in this subsection.

We have chosen to write the high level simulation code using the PYTHON language. PYTHON is a general purpose language, is geared towards readability, and is well supported by a comprehensive library and wide user base (including astronomers). Specifically PYTHON interfaces well with a modern interferometric toolbox, MEQTREES, as well as our data formats of choice: FITS for image cubes and the MEASUREMENT SET¹ MS for visibilities. Although the higher level functionality is written in PYTHON, the bulk of the computational load (MS and visibility generation) is called through the faster C++ language. We use MS as our data format as it is directly accessible via the PYRAP library and is the data format used by MEQTREES which performs the visibility generation and pointing error simulation. Although in the mm-VLBI subfield other data formats are currently still more popular than the MS, i.e. UVFITS or IOFITS, with the completion of ALMA, the MS format should become the next modern data format and already is used at the Joint Institute for VLBI in Europe (JIVE).

To create a flexible and modular structure necessary to be able to run a diversity of experiments, the software implementation is divided into 2 components:

- an object-oriented framework into which is programmed the logic of each individual step in the signal propagation chain,
- a driver script which initialises the most abstract class in the framework with the required inputs and determines the signal propagation chain relevant to that particular pipeline.

The conceptual flow diagram of one realisation of a MEQSILHOUETTE simulation pipeline is shown in Fig. 6. To emphasise, the framework is not restricted to this sequence of operations, allowing the exact pipeline to be quite general. This flexibility is made possible through the use of *Object-Orientation*, which will be elaborated on later.

¹<https://casa.nrao.edu/Memos/229.html>

All inputs to the simulator are specified by a configuration file, containing a dictionary, which is the sole input to the driver script. This dictionary contains everything needed by the pipeline to determine the particular observation configuration (frequency, bandwidth, start time, etc), which signal corruption implementation should be employed and where the sky model and antenna table are located in the filesystem. Antenna table is in the CASA format, and can readily be created or altered using the PYRAP library using the station coordinates. The primary accepted sky model is a time-ordered list of FITS images, where each image represents the source total intensity over a time interval $\Delta t_{\text{src}} = t_{\text{obs}}/N_{\text{src}}$, where t_{obs} is the observation length and N_{src} is the number of source images. Currently the pipeline only supports total intensity and the conversion of the pipeline to support full stokes is discussed in section ???. A variation of the pipeline has also been written which uses a parametric source model consisting of Gaussians or point sources as the sky model. This functionality was needed for the simulation of pointing errors as the MEQTREES beams model does not support the FITS sky model.

The primary outputs of the pipeline are an interferometric dataset in MS format along with the closure phases (including uncertainties) and a dirty and/or deconvolved image. The modular structure of the pipeline allows for additional imaging and deconvolution algorithms to be easily appended to the final data processing steps. Noting that there are other data formats widely used in mm-VLBI, we make use of the CASA task for conversion to UVFITS. As the pipeline is easily flexible other data products can be easily produced as needed e.g. polarisation ratios or time-frequency averaged data.

An important step to reproduce realistic observations is to be able create a comprehensive MS with arbitrary scan lengths, start times, channel and bandwidth structure. This is performed using the SIMMS² tool. SIMMS provides an easy to use command line interface to construct a general MS, given the appropriate antenna table. The call to SIMMS is located within the driver script.

In order to make the framework as clean and modular as possible we have made extensive use of object orientation. The first major class, *SimpleMS*, was intended to abstract and modularise the MS and MS-only derived attributes (e.g. visibility data and station positions) and methods (e.g. functions to calculate station elevations and closure phases) as well as expose these attributes and methods more efficiently than following PYRAP procedures which become verbose when used frequently. This is especially

²<https://github.com/radio-astro/simms>

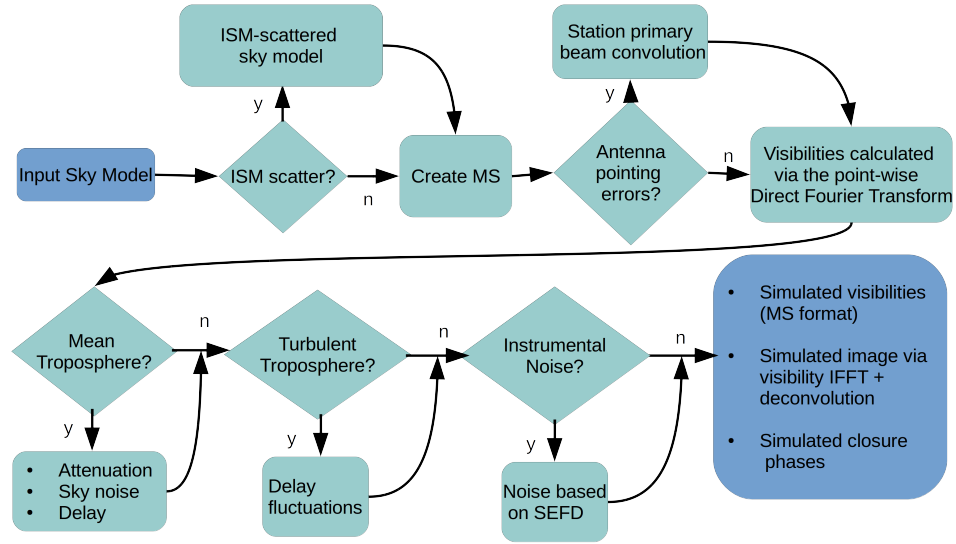


Figure 2.1: Flow diagram showing basic sequence of a MEQSILHOUETTE simulation pipeline. The specific sequence is determined by the driver script whereas the logic of each step is contained in an object-oriented framework. The details of the station information, observation strategy, tropospheric and ISM conditions are specified in a user-defined input configuration file. The pipeline is extendable, allowing any additional, arbitrary Jones matrices to be incorporated.

useful to access baseline-index quantities.

The second MS-related class, *TropMS*, handles the calculations relevant to tropospheric and thermal noise corruptions. This class is a child of *SimpleMS* and is initialised with weather and station information. Note that a child contains all the methods and attributes of its parent. This allows the tropospheric corruption implementation to use, whilst being separated from, the core MS functionality. The details of the tropospheric corruption is provided in section 4.2.

The third MS-related class, *SimCoordinator*, is a child of the *TropMS* class. *SimCoordinator* is designed to make arbitrary simulations easy and efficient to construct and execute on a high level. It is the only MS class directly initialised in the driver script and hence the low level functionality and attributes of its parents are abstracted from the user. In addition to inherited functionality, *SimCoordinator* can call the ISM-scattering task (see subsection 4.1), and MEQTREES simulation functionality. Specifically within MEQTREES we make use of the *turbo-sim* script which evaluates the RIME to generate visibilities and to simulate antenna pointing errors (see section 4.3, where the visibilities are calculated through direct evaluation of the Fourier Transform at each UVW coordinate in the dataset. MEQTREES allows its tasks to be called from PYTHON scripts and so can be easily pipelined.

2.2.1 ISM scattering

As described in section ?? observations of Sgr A* at sub(mm) is subject to ISM scattering in the strong scattering regime. Due to the size of Sgr A* at mm-wavelengths, a single epoch observation of the scattering screen is further defined as falling into the *average regime*, wherein diffractive scintillation is averaged out but refractive scintillation is still present. As mm-VLBI observations can resolve the scatter-broadened image of Sgr A*, an implementation of scattering is needed which approximates the subtle changes in its extended source structure. Such an approximation has been implemented in the PYTHON-based SCATTERBRANE³ package, and is based on ?]. In this algorithm a phase screen is created based on the two dimensional spatial power spectrum [see ? , Appendix C] which incorporates inner and outer turbulent lengths scales. With the screen generated, the original image is scattered according to equation 21. In practice equation 21 is implemented using an interpolation function which is modified by the values on the phase

³<http://krosenfeld.github.io/scatterbrane>

Table 2.1: The list of the parameters, aside from the source model, needed to initialise and run SCATTERBRANE. Time variability is made possible as N_{rmpix} can be a 2-tuple (i.e. a rectangular screen can be created) and the task implementing the scattering has an argument to translate the square subsection of the screen used when scattering.

r_0	N_{pix}
r_{in}	principal angle
r_{out}	anisotropy of scattering kernel
D_{os}	λ
R	β
screen resolution	

screen. SCATTERBRANE allows variation in all parameters (see table 4.1) associated with the scattering screen which is essential as aspects of the scattering towards the galactic centre are still unconstrained.

We include the SCATTERBRANE software, which has already yielded important context for mm-VLBI observations towards Sgr A* [e.g. ?], within the MEQSILHOUETTE framework. Our ISM module interfaces the SCATTERBRANE code within an interferometric simulation pipeline. This module enables simultaneous use of time-variable ISM scattering and time-variable intrinsic source structure within a single framework. The user is able to select a range of options relating to the time-resolution and epoch interpolation/averaging of both. By default, if the time resolution chosen to sample the source variability Δt_{src} and screen variability Δt_{ism} are unequal, we set

- $\Delta t_{\text{ism}} = \Delta t_{\text{src}}$ if $\Delta t_{\text{src}} < \Delta t_{\text{ism}}$
- $\Delta t_{\text{ism}} = R(\frac{\Delta t_{\text{src}}}{\Delta t_{\text{ism}}})\Delta t_{\text{src}}$ if $\Delta t_{\text{src}} > \Delta t_{\text{ism}}$,

where R rounds the fraction to the nearest integer. This modification to the ISM sampling resolution avoids interpolation between different snapshots of the intrinsic source structure.

2.2.2 Atmospheric corruption simulator

Our focus in this module is to model the three primary, interrelated (see section 2.3.1) observables which are the most relevant to mm-VLBI: turbulence-driven fluctuations in the visibility phase $\delta\phi$; signal attenuation due to the atmospheric opacity τ ; and the increase in system temperature due to atmospheric emission at a brightness temperature T_{atm} . Our approach is to model

these observables as being separable into mean and turbulent components which are simulated independently. The mean tropospheric simulation module performs radiative transfer with a detailed model of the electromagnetic spectrum of each atmospheric constituent. The turbulent simulation module takes a scattering approach to account for the decoherence that results from power-law turbulence.

As described in section 2.3.3, we use the ATM package to perform radiative transfer through the realisation of the mean atmosphere. In order to calculate atmospheric temperature and pressure profiles, ATM is input several station dependent parameters, namely, ground temperature and pressure, PWV depth, water vapour scale height, tropospheric lapse rate and altitude. The lapse rate refers to the linear relation at which temperature decreases with height. Through experimentation, we have found that the first 3 variables most significantly effect the results of the simulation and opt to keep the latter variables at their default values which were set for application to ALMA. The outputs, relevant to our application is the opacity, time delay and atmospheric brightness temperature. Both opacity and time delay are separated into wet (water) and dry components. These outputs are calculated for a input list of frequencies. We perform this calculation using representative climate conditions taken from the literature, where the calculation is repeated for each station. This final step is to account for elevation effects by multiplying by the airmass.

Following from section 2.3.4, we derive a weak scattering formalism to calculate station dependent visibilities phase variations which result from observing through a turbulent troposphere. Specifically we simulate random walks in visibility phase with variance given by equation 37 for each antenna. These phase-time series are combined to form a multiplicative complex gain corruption, with amplitude of unity i.e. a diagonal Jones matrix. In section ?? we explore the effect of the mean and turbulent atmosphere on observables.

2.2.3 Pointing error simulator

To simulate pointing errors, we use the implementation built into the MEQTREES turbo-sim task. This functionality includes a station primary beam models into the RIME which can be a sinc or Gaussian function or the analytic WSRT beam model. The standard beam model which we will make use of later is the analytic WSRT beam model [34]

$$E(l, m) = \cos^3(C\nu\rho), \quad \rho = \sqrt{\delta l_p^2 + \delta m_p^2} \quad (2.1)$$

where C is a constant, with value $C \approx 130 \text{ GHz}^{-1}$. Note that the power beam EE^H becomes \cos^6 , resulting in a FWHM = 6.5 arcsec at 230 GHz. However there is not much difference between the different beam models up until the first null. One drawback of the MEQTREES implementation is that it is incompatible with the FITS format and so we are limited to point and Gaussian parameteric sources for the pointing error simulations. However this is not a big issue as the pointing error should be constant across the FOV and hence source structure observable with mm-VLBI is unimportant to any pointing error analysis.

Furthermore turbo-sim allows constant offset or time variable primary beam, where the time variability can be either an up-to-third order polynomial or a sinusoidal function. We have opted to incorporate only the sinusoidal variability for simplicity. To simulate stochastic variability i.e. pointing error due to slew between calibrator and source, we use a constant offset which is resampled per user-specified time interval. In section ?? we demonstrate the effect of constant, sinusoidally variable and stochastically variable pointing errors on the LMT which is the EHT station with the most narrow beam, and could be used as a referenced station due to its centrality the array.

2.3 RODRIGUES interface

For community use, we host the online, RODRIGUES, interface, found at <http://rodrigues.meqtrees.net/>. Each of the components of the simulator run in Docker containers. **Looks like the infrastructure is going to change, re: discussions with Gijis and Sphe, so going to wait before writing this.

Bibliography

- [1] J. W. Armstrong, B. J. Rickett, and S. R. Spangler. Electron density power spectrum in the local interstellar medium. *ApJ*, 443:209–221, April 1995.
- [2] F. K. Baganoff, M. W. Bautz, W. N. Brandt, G. Chartas, E. D. Feigelson, G. P. Garmire, Y. Maeda, M. Morris, G. R. Ricker, L. K. Townsley, and F. Walter. Rapid X-ray flaring from the direction of the supermassive black hole at the Galactic Centre. *Nature*, 413:45–48, September 2001.
- [3] M. Born and E. Wolf. *Principles of Optics Electromagnetic Theory of Propagation, Interference and Diffraction of Light*. 1980.
- [4] G. C. Bower, H. Falcke, R. M. Herrnstein, J.-H. Zhao, W. M. Goss, and D. C. Backer. Detection of the Intrinsic Size of Sagittarius A* Through Closure Amplitude Imaging. *Science*, 304:704–708, April 2004.
- [5] G. C. Bower, W. M. Goss, H. Falcke, D. C. Backer, and Y. Lithwick. The Intrinsic Size of Sagittarius A* from 0.35 to 6 cm. *ApJ*, 648:L127–L130, September 2006.
- [6] C. D. Brinkerink, C. Müller, H. Falcke, G. C. Bower, T. P. Krichbaum, E. Castillo, A. T. Deller, S. S. Doeleman, R. Fraga-Encinas, C. Goddi, A. Hernández-Gómez, D. H. Hughes, M. Kramer, J. León-Tavares, L. Loinard, A. Montaña, M. Mościbrodzka, G. N. Ortiz-León, D. Sanchez-Arguelles, R. P. J. Tilanus, G. W. Wilson, and J. A. Zensus. Asymmetric structure in Sgr A* at 3 mm from closure phase measurements with VLBA, GBT and LMT. *MNRAS*, 462:1382–1392, October 2016.
- [7] C. L. Carilli and M. A. Holdaway. Tropospheric phase calibration in millimeter interferometry. *Radio Science*, 34:817–840, 1999.

- [8] C. E. Coulman. Fundamental and applied aspects of astronomical 'seeing'. *ARA&A*, 23:19–57, 1985.
- [9] E. I. Curtis, B. Nikolic, J. S. Richer, and J. R. Pardo. Atmospheric dispersion and the implications for phase calibration. *ArXiv e-prints*, December 2009.
- [10] S. S. Doeleman, V. L. Fish, A. E. Broderick, A. Loeb, and A. E. E. Rogers. Detecting Flaring Structures in Sagittarius A* with High-Frequency VLBI. *ApJ*, 695:59–74, April 2009.
- [11] S. S. Doeleman, Z.-Q. Shen, A. E. E. Rogers, G. C. Bower, M. C. H. Wright, J. H. Zhao, D. C. Backer, J. W. Crowley, R. W. Freund, P. T. P. Ho, K. Y. Lo, and D. P. Woody. Structure of Sagittarius A* at 86 GHz using VLBI Closure Quantities. *AJ*, 121:2610–2617, May 2001.
- [12] S. S. Doeleman, J. Weintroub, A. E. E. Rogers, R. Plambeck, R. Freund, R. P. J. Tilanus, P. Friberg, L. M. Ziurys, J. M. Moran, B. Corey, K. H. Young, D. L. Smythe, M. Titus, D. P. Marrone, R. J. Cappallo, D. C.-J. Bock, G. C. Bower, R. Chamberlin, G. R. Davis, T. P. Krichbaum, J. Lamb, H. Maness, A. E. Niell, A. Roy, P. Strittmatter, D. Werthimer, A. R. Whitney, and D. Woody. Event-horizon-scale structure in the supermassive black hole candidate at the Galactic Centre. *Nature*, 455:78–80, September 2008.
- [13] V. L. Fish, S. S. Doeleman, C. Beaudoin, R. Blundell, D. E. Bolin, G. C. Bower, R. Chamberlin, R. Freund, P. Friberg, M. A. Gurwell, M. Honma, M. Inoue, T. P. Krichbaum, J. Lamb, D. P. Marrone, J. M. Moran, T. Oyama, R. Plambeck, R. Primiani, A. E. E. Rogers, D. L. Smythe, J. SooHoo, P. Strittmatter, R. P. J. Tilanus, M. Titus, J. Weintroub, M. Wright, D. Woody, K. H. Young, and L. M. Ziurys. 1.3 mm Wavelength VLBI of Sagittarius A*: Detection of Time-variable Emission on Event Horizon Scales. *ApJ*, 727:L36, February 2011.
- [14] V. L. Fish, S. S. Doeleman, A. E. Broderick, A. Loeb, and A. E. E. Rogers. Detecting Changing Polarization Structures in Sagittarius A* with High Frequency VLBI. *ApJ*, 706:1353–1363, December 2009.
- [15] V. L. Fish, M. D. Johnson, R.-S. Lu, S. S. Doeleman, K. L. Bouman, D. Zoran, W. T. Freeman, D. Psaltis, R. Narayan, V. Pankratius, A. E. Broderick, C. R. Gwinn, and L. E. Vertatschitsch. Imaging an Event Horizon: Mitigation of Scattering toward Sagittarius A*. *ApJ*, 795:134, November 2014.

- [16] R. Genzel, R. Schödel, T. Ott, A. Eckart, T. Alexander, F. Lacombe, D. Rouan, and B. Aschenbach. Near-infrared flares from accreting gas around the supermassive black hole at the Galactic Centre. *Nature*, 425:934–937, October 2003.
- [17] J. Goodman and R. Narayan. The Shape of a Scatter Broadened Image - Part Two - Interferometric Visibilities. *MNRAS*, 238:995, June 1989.
- [18] C. R. Gwinn, M. D. Johnson, J. E. Reynolds, D. L. Jauncey, A. K. Tzioumis, H. Hirabayashi, H. Kobayashi, Y. Murata, P. G. Edwards, S. Dougherty, B. Carlson, D. del Rizzo, J. F. H. Quick, C. S. Flanagan, and P. M. McCulloch. Size of the Vela Pulsar’s Emission Region at 18 cm Wavelength. *ApJ*, 758:7, October 2012.
- [19] C. R. Gwinn, Y. Y. Kovalev, M. D. Johnson, and V. A. Soglasnov. Discovery of Substructure in the Scatter-broadened Image of Sgr A*. *ApJ*, 794:L14, October 2014.
- [20] D. C. Hogg, F. O. Guiraud, and M. T. Decker. Measurement of excess radio transmission length on earth-space paths. *A&A*, 95:304–307, March 1981.
- [21] M. D. Johnson, V. L. Fish, S. S. Doeleman, A. E. Broderick, J. F. C. Wardle, and D. P. Marrone. Relative Astrometry of Compact Flaring Structures in Sgr A* with Polarimetric Very Long Baseline Interferometry. *ApJ*, 794:150, October 2014.
- [22] R. G. Lane, A. Glindemann, and J. C. Dainty. Simulation of a Kolmogorov phase screen. *Waves in Random Media*, 2:209–224, July 1992.
- [23] O. P. Lay. The temporal power spectrum of atmospheric fluctuations due to water vapor. *A&AS*, 122, May 1997.
- [24] R.-S. Lu, T. P. Krichbaum, A. Eckart, S. König, D. Kunneriath, G. Witzel, A. Witzel, and J. A. Zensus. Multiwavelength VLBI observations of Sagittarius A*. *A&A*, 525:A76, January 2011.
- [25] R.-S. Lu, F. Roelofs, V. L. Fish, H. Shiokawa, S. S. Doeleman, C. F. Gammie, H. Falcke, T. P. Krichbaum, and J. A. Zensus. Imaging an Event Horizon: Mitigation of Source Variability of Sagittarius A*. *ApJ*, 817:173, February 2016.
- [26] J.-P. Macquart and G. C. Bower. Understanding the Radio Variability of Sagittarius A*. *ApJ*, 641:302–318, April 2006.

- [27] C. R. Masson. Atmospheric Effects and Calibrations. 59:87–95, 1994.
- [28] L. Meyer, T. Do, A. Ghez, M. R. Morris, G. Witzel, A. Eckart, G. Bélanger, and R. Schödel. A 600 Minute Near-Infrared Light Curve of Sagittarius A*. *ApJ*, 688:L17, November 2008.
- [29] J. D. Monnier. Phases in interferometry. *New A Rev.*, 51:604–616, October 2007.
- [30] R. Narayan. The Physics of Pulsar Scintillation. *Philosophical Transactions of the Royal Society of London Series A*, 341:151–165, October 1992.
- [31] R. Narayan and J. Goodman. The shape of a scatter-broadened image. I - Numerical simulations and physical principles. *MNRAS*, 238:963–1028, June 1989.
- [32] B. Nikolic, R. C. Bolton, S. F. Graves, R. E. Hills, and J. S. Richer. Phase correction for ALMA with 183 GHz water vapour radiometers. *A&A*, 552:A104, April 2013.
- [33] J. R. Pardo, J. Cernicharo, and E. Serabyn. Atmospheric transmission at microwaves (ATM): an improved model for millimeter/submillimeter applications. *IEEE Transactions on Antennas and Propagation*, 49:1683–1694, December 2001.
- [34] A. Popping and R. Braun. The standing wave phenomenon in radio telescopes. Frequency modulation of the WSRT primary beam. *A&A*, 479:903–913, March 2008.
- [35] D. Psaltis, F. Özel, C.-K. Chan, and D. P. Marrone. A General Relativistic Null Hypothesis Test with Event Horizon Telescope Observations of the Black Hole Shadow in Sgr A*. *ApJ*, 814:115, December 2015.
- [36] S. J. Radford and M. A. Holdaway. Atmospheric conditions at a site for submillimeter-wavelength astronomy. 3357:486–494, July 1998.
- [37] A. E. E. Rogers, S. S. Doeleman, and J. M. Moran. Fringe detection methods for very long baseline arrays. *AJ*, 109:1391–1401, March 1995.
- [38] Z.-Q. Shen, K. Y. Lo, M.-C. Liang, P. T. P. Ho, and J.-H. Zhao. A size of ~ 1 AU for the radio source Sgr A* at the centre of the Milky Way. *Nature*, 438:62–64, November 2005.

- [39] A. R. Thompson, J. M. Moran, and G. W. Swenson, Jr. Interferometry and Synthesis in Radio Astronomy, 2nd Edition. 2001.
- [40] R. N. Treuhaft and G. E. Lanyi. The effect of the dynamic wet troposphere on radio interferometric measurements. *Radio Science*, 22:251–265, April 1987.
- [41] J. M. Wrobel and R. C. Walker. Sensitivity. 180:171, 1999.
- [42] F. Yusef-Zadeh, D. Roberts, M. Wardle, C. O. Heinke, and G. C. Bower. Flaring Activity of Sagittarius A* at 43 and 22 GHz: Evidence for Expanding Hot Plasma. *ApJ*, 650:189–194, October 2006.